Additive Manufacturing 12 (2016) 282–290

Contents lists available at ScienceDirect

Additive Manufacturing

journal homepage: www.elsevier.com/locate/addma

Prediction of porosity in metal-based additive manufacturing using spatial Gaussian process models

G. Tapia[a], A.H. Elwany[a,*], H. Sang[b]

[a] Department of Industrial and Systems Engineering, Texas A&M University, College Station, TX, United States
[b] Department of Statistics, Texas A&M University, College Station, TX, United States

ARTICLE INFO

Article history:
Received 12 December 2015
Received in revised form 20 February 2016
Accepted 8 May 2016
Available online 19 May 2016

Keywords:
Additive manufacturing
Selective laser melting
17-4 PH stainless steel
Spatial statistics
Gaussian process

ABSTRACT

Additive manufacturing (AM) is a set of emerging technologies that can produce physical objects with complex geometrical shapes directly from a digital model. With many unique capabilities, such as design freedom, it has recently gained increasing attention from researchers, practitioners, and public media. However, achieving the full potential of AM is hampered by many challenges, including the lack of predictive models that correlate processing parameters with the properties of the processed part. We develop a Gaussian process-based predictive model for the learning and prediction of the porosity in metallic parts produced using selective laser melting (SLM – a laser-based AM process). More specifically, a spatial Gaussian process regression model is first developed to model part porosity as a function of SLM process parameters. Next, a Bayesian inference framework is used to estimate the statistical model parameters, and the porosity of the part at any given setting is predicted using the Kriging method. A case study is conducted to validate this predictive framework through predicting the porosity of 17-4 PH stainless steel manufacturing on a ProX 100 selective laser melting system.

1. Introduction

Additive manufacturing (AM) has recently gained increased attention by researchers, practitioners, and even public media [1–3]. It is regarded by some as a potential game changer, especially with the advent of AM technologies that can process advanced metallic materials and alloys such as stainless steel [4–6], Ti-6Al-4V [7,8], and nickel-based alloys [9]. In contrast to the limited application of polymer-based AM in producing visualization or functional prototypes to accelerate product development in the early 1980s, metal-based AM is now used to produce parts for direct use such as the fuel nozzle that GE Aviation will use in their LEAP engine [10,11], Lockheed's blead air leak detector [12], and biomedical cranial and hip implants [13–15].

There are many obstacles that still hamper the widespread adoption of metal-based AM as a mainstream manufacturing method. These include for example part quality, repeatability, and the lack of material and process standards, among others. Many recent road mapping efforts have been conducted by academic and industrial stakeholders to identify technological barriers, desired capabilities, and research efforts needed to unlock the opportunities that AM has to offer (see for example the roadmap for additive manufacturing [16] and NIST's measurement science roadmap for metal-based additive manufacturing [17]). These efforts have been instrumental in providing guidance and vision for researchers, and their impact on the advancement of AM technologies is starting to be realized [18].

One of the missing and highly desired capabilities, aligned both with the vision of these road mapping efforts as well as industrial needs, is providing modeling and simulation capabilities that decrease the need for real-world testing and provides designers with predictive capabilities to optimize part and process design [17, p. 35]. This is important due to the high costs associated with experiments and testing needed to achieve the desired part properties. It is further complicated by the fact that most metal-based AM technologies involve many process parameters and complex physical transformations that influence the properties of the final part.

In this work, we develop a predictive modeling framework based on Gaussian process (GP) models to predict the resulting density (or porosity) in parts manufactured using selective laser melting (SLM) as a function of the processing parameters. SLM is a laser-based metal AM process that produces physical parts directly from a computer digital model, layer upon layer, by selective fusing metallic powder using a high energy laser beam [19]. Porosity is a common

* Corresponding author.
E-mail addresses: gustapia06@tamu.edu (G. Tapia), elwany@tamu.edu (A.H. Elwany), huiyan@stat.tamu.edu (H. Sang).

http://dx.doi.org/10.1016/j.addma.2016.05.009
2214-8604/

defect that has been reported in SLM parts, resulting in compromising the mechanical properties and performance of the part. It is well established that excessive concentration of pores in the part's structure could reduce tensile strength, ductility and fatigue properties [20]. Multiple mechanisms contribute to porosity in SLM parts. These include shrinkage, gas entrapment during solidification [21,22], and adhesion of partially molten particles to surfaces between layers [23]. Additionally, depending on the wettability, capillary forces and surface tension of the melt pool, a defect known as "balling" can occur which results in uneven subsequent powder layers and, consequently, pores upon processing of the material [24].

Selection of multiple processing parameters such as laser power, scanning speed, and layer thickness [25] impact part porosity. The majority of existing efforts rely on extensive round-robin testing for selecting parameter combinations that maximize part density and minimize porosity. In contrast, we develop a systematic approach that enables accurate prediction of porosity at any given parameter combination while keeping the number of costly experiments to a minimum. In particular, we develop a GP regression model to express part porosity as a flexible stochastic function of SLM processing parameters, and use a Bayesian inference procedure to estimate the model parameters and subsequently predict porosity.

Gaussian process models have been widely used in Bayesian nonparametric statistics to specify prior distributions on function spaces due to their desirable mathematical and computational properties, and ability to incorporate a wide range of smoothness assumptions [26]. Examples include spatial modeling [27], computer model emulation [28,29], image analysis [30], and supervised classification and prediction in machine learning [31]. The popularity of such processes are mainly due to their many attractive mathematical and computational properties, and their flexibility and richness in modeling dependence among data observed in space. Our work is among the first to introduce spatial GP models to addressing the modeling and prediction of metal-based AM processes. We validate our methodology using real-world data that we acquired from building 17-4 PH stainless steel test coupons using SLM.

The paper is organized as follows: Section 2 surveys relevant literature related to metal-based AM and statistics, with emphasis on works that studied the manufacturing of 17-4 PH stainless steel. In Section 3, we define the problem and formulate a GP regression model for predicting porosity in metallic parts produced using SLM. We then present a Bayesian inference method for estimating the parameters of this model, and use these estimated model parameters for prediction in Sections 4 and 5, respectively. A real-world case study is conducted in Section 6 to validate the proposed predictive framework using data from the production of 17-4 PH stainless steel samples on a commercial SLM system housed in the authors' laboratory. Finally, concluding remarks and directions for future research are outlined in Section 7.

2. Literature review

Additive manufacturing (AM) technologies are currently categorized into 7 distinct categories according to the material being used and the mechanism with which each layer is produced [32]. The two most common process categories used for producing metallic parts are powder bed fusion (PBF) and directed energy deposition (DED) processes. This is primarily due to their ability of producing dense metallic parts without the need for significant post processing [19]. Both categories share the common aspect that parts are produced by melting metallic powder using an high energy source (commonly a laser or electron beam). The key difference between them is the powder feed mechanism: in PBF, the energy source melts powder placed in a powder bed, whereas in DED the powder is coaxially fed with the energy source. Our focus in this work is on selective laser melting (SLM) which is a class of PBF processes that fuses metallic powder using a laser beam. Excellent overviews and summaries of different AM process categories and technologies are provided by Wohlers [10] and Gibson et al. [23].

The body of the literature on SLM is quite large, studying the fabrication of different metallic materials such titanium alloys [7,33,34], aluminum alloys [35–37], and nickel alloys [38,9,39]. We consider the SLM of steel in this study, which has been frequently studied. Some of the investigated steel alloys include austenitic 316L stainless steel [40,6,41,42], H13 tool steel [43,44], and maraging steel [45,46]. Our choice of precipitation hardening martensitic steel (17-4 PH) for this study has two main motivations: first, this alloy has wide used in industrial applications that require a combination of high strength and a moderate level of corrosion resistance [47,48]; and second, it is commercially available in gas atomized powder form for SLM applications.

Most of the works on the SLM of 17-4 PH steel investigate its manufacturability and analyze the properties of the fabricated parts. For example, Facchini et al. [49] analyze the microstructure and Kumar and Kruth [50] study the wear behavior of SLM-fabricated 17-4 steel parts. Murr et al. [51] provide a good review on efforts in processing 17-4 PH steel and other metallic alloys using laser- and electron beam-based AM, with a focus on reporting the microstructure and phase structures.

Very few works follow systematic approaches for assessing the impact of SLM process parameters on the properties of the end part. One example is the work by Averyanova et al. [4] who use a fractional factorial approach to assess the impact of process and material parameters on the dimensional stability and surface roughness of a single layer 17-4 PH. The effect of the optimized process parameters on the microstructure of the final part is subsequently studied in [52]. Spierings et al. [53] employ full-factorial experimental design examine the effect of energy density on the density and elasticity of 17-4 PH specimens. Gu et al. [54] and Averyanova and Bertrand [55] also study the effect of process parameters on the density of 17-4 PH specimens, however the values of process parameters were arbitrarily selected.

In contrast to the above works, we construct a predictive model that provides a systematic framework for predicting the porosity (or density) of SLM-fabricated 17-4 PH steel motivated from Gaussian process models widely used in spatial statistics.

Spatial statistics started as an ad-hoc field with few works dated as back as the early 1900s, however strong theoretical research has been developed since the 1950s, with applications focused on mining, agriculture and forestry [56]. It experienced significant growth over the past two decades particularly with the development of low-cost high-speed computing [56,57], extending its application domains into other fields such as healthcare, social and environmental geography, oil and gas exploration, fisheries and animal migration, socioeconomics and econometrics, among others [58]. To date, fewer works use spatial models in manufacturing applications. Yang and Jackman [59] scan points on the surface of a workpiece and use a spatial model to predict and estimate form (geometry) errors. Colosimo et al. [60] propose a process control method that combines control charts with spatial correlated noise, and apply this method to monitor the roundness geometrical tolerance for parts produced by turning. A similar hybrid approach encompassing spatial information with control charts is used by Collica et al. [61] for quality control in the manufacturing of integrated circuits. Hsu and Chien [62] develop a data mining approach that integrates spatial statistics with adaptive neural networks to identify patterns of defects in semiconductor manufacturing. The authors use a case study to demonstrate their approach can be used to provide information on production defects and their root-causes.

Pegel et al. [63] develop a spatial model to investigate and quantify the morphology, content and location of carbon nanotubes inside polymer composites using TEM imaging.

To the best of our knowledge, the current work represents a first effort on utilizing powerful stochastic process tools in spatial statistics for providing predictive capabilities in metal-based AM.

3. Predictive Gaussian process regression model

We start by developing a GP regression model to investigate the behavior of part porosity as a function of SLM process parameters. There are many controllable process parameters in SLM processes [25]. The parameters that have been reported to possess the highest influence on the porosity of SLM parts include: laser power, laser scanning speed, powder layer thickness, hatch distance (the distance between two successive passes of the laser beam in the same layer) and laser beam size [64]. Most of the works in the literature relied on tools of experimental design, ANOVA, and Taguchi's method to identify these parameters as the most influential (see for example [65,66,4,67–72]). In this study, we focus our attention on the effect of laser power (P) and scanning speed (v), while the other parameters (hatch distance, layer thickness and beam size) will be kept constant. However, we remark that the GP modeling tool we develop below is a general approach that can be easily extended to the case with more than two input parameters, and can also be used to identify most influential parameters if combined with statistical variable selection methods.

We model the resulting part porosity in the defined $P-v$ two-dimensional space using the following Gaussian process regression model:

$$Y(\mathbf{s}) = \mu(\mathbf{s}) + \omega(\mathbf{s}) + \epsilon(\mathbf{s}) \tag{1}$$

where $\mathbf{s} \in \mathbb{D} \subset \mathbb{R}^2$ represents a location over a bounded study region $\mathbb{D}$ in the two-dimensional $P-v$ space, defined by the pair (x_P, x_v) with x_P and x_v representing values of the laser power and scanning speed, respectively. The response $Y(\mathbf{s})$ is the porosity at location $\mathbf{s}$, and $\mu(\mathbf{s})$ is the mean function denoting the average porosity at location $\mathbf{s}$. $\omega(\mathbf{s})$ is a spatial random effect capturing the dependence between two different locations $\mathbf{s}_i, \mathbf{s}_j \in \mathbb{D}$ within the $P-v$ space that is unexplained by the mean function. A flexible and common choice of modeling $\omega(\mathbf{s})$ is to assume a Gaussian Process with zero mean and covariance function C: GP($\mathbf{0}, C(\mathbf{s}_i, \mathbf{s}_j; \boldsymbol{\theta})$), where $C(\mathbf{s}_i, \mathbf{s}_j; \boldsymbol{\theta})$ defines the covariance between $\omega(\mathbf{s}_i)$ and $\omega(\mathbf{s}_j)$, and $\boldsymbol{\theta}$ is a vector of parameters defining the covariance function. Finally, $\epsilon(\mathbf{s})$ is the nugget effect capturing measurement error, and is often assumed to be independent and identically normally distributed with mean 0 and variance τ^2 for every $\mathbf{s} \in \mathbb{D}$ [73].

3.1. Mean function

The mean function is specified as $\mu(\mathbf{s}) = \mathbf{X}^\top(\mathbf{s})\boldsymbol{\beta}$, where $\mathbf{X}(\mathbf{s})$ is a $d \times 1$ vector of spatially referenced explanatory variables observed at $\mathbf{s}$ and $\boldsymbol{\beta}$ is the vector of regression coefficients. We model $\mu(\mathbf{s})$ as a second order regression with interactions and an intercept:

$$\mu(\mathbf{s}) = \beta_0 + \beta_1 x_P + \beta_2 x_v + \beta_3 x_P x_v + \beta_4 x_P^2 + \beta_5 x_v^2 \tag{2}$$

where x_P and x_v are the coordinates at location $\mathbf{s}$.

3.2. Covariance function

Several covariance functions have been developed in the literature on geostatistics, most of which were specifically developed for applications in geographical spaces. In other words, in the $\mathbb{R}^2$ space with both dimensions having same physical units (distance). The Euclidean distance was typically used as a measure of the distance between two points. The challenge in our model is the fact that the two dimensions P and v have different units (Watts and mm/s, respectively), and thus the Euclidean distance is not relevant. To overcome this challenge, we have based our covariance function on the widely adopted class of Matérn covariance functions [56] due to its richness and simplicity, and conducted re-parameterization to adapt it to our application:

$$C(\mathbf{z}; \boldsymbol{\theta}) = C(\mathbf{s}_i, \mathbf{s}_j; \boldsymbol{\theta}) = \sigma^2 \frac{Q^\kappa K_\kappa(Q)}{\Gamma(\kappa) 2^{\kappa-1}} \tag{3}$$

The covariance function defined in the equation above has two main components: a variance component σ^2, and the correlation function represented by the quantity in the fraction. κ is the function smoothness parameter; $\mathbf{z} = \mathbf{s}_i - \mathbf{s}_j$ is a spatial separation vector between two locations $\mathbf{s}_i$ and $\mathbf{s}_j$. We define $Q = \sqrt{\left(\frac{z_P}{\lambda_P}\right)^2 + \left(\frac{z_v}{\lambda_v}\right)^2}$ as our measure of spatial closeness between two locations (i.e. a variation of Euclidean distance), with z_P and z_v being the coordinates of $\mathbf{z}$. $K_\kappa(\cdot)$ is the modified Bessel function of the second kind of order κ, and $\boldsymbol{\theta} = \{\sigma^2, \lambda_P, \lambda_v\}$ is the set of covariance function parameters that are to be estimated.

4. Bayesian estimation of the model parameters

We follow a Bayesian framework to estimate the parameters of the statistical model. Let $\boldsymbol{\Omega} = \{\boldsymbol{\beta}, \boldsymbol{\theta}, \tau^2\}$ denote collectively the model parameters, $\mathbf{Y} = [Y(\mathbf{s}_1), \ldots, Y(\mathbf{s}_n)]^\top$ denote a vector of n observed response variables at a collection of spatial points $\mathrm{S} = \{\mathbf{s}_1, \ldots, \mathbf{s}_n\}$ from the conducted initial experiments, and $\mathbb{X} = [\mathbf{X}(\mathbf{s}_1), \ldots, \mathbf{X}(\mathbf{s}_n)]^\top$ denote the matrix of associated regression covariates in the mean function.

In a Bayesian approach, model parameters are treated as random variables that follow a joint prior distribution $p(\boldsymbol{\Omega})$. Next, the posterior distribution of the parameters given observed data, $p(\boldsymbol{\Omega}|\mathbf{Y})$, is computed using Bayes' rule:

$$p(\boldsymbol{\Omega}|\mathbf{Y}) \propto p(\mathbf{Y}|\boldsymbol{\Omega}) \times p(\boldsymbol{\Omega}) \tag{4}$$

where $p(\mathbf{Y}|\boldsymbol{\Omega})$ is the likelihood function, which represents the conditional distribution of the response $\mathbf{Y}$ given the model parameters $\boldsymbol{\Omega}$. Upon computing the posterior distribution $p(\boldsymbol{\Omega}|\mathbf{Y})$, it can be used to make inference about the parameters.

From the model given by Eq. (1), and the mean and covariance functions defined in Eqs. (2) and (3), respectively, it results that the likelihood function follows an n-dimension multivariate normal distribution given by:

$$p(\mathbf{Y}|\boldsymbol{\Omega}) \sim \mathrm{MVN}(\mathbb{X}\boldsymbol{\beta},\ \boldsymbol{\Sigma}(\boldsymbol{\theta}) + \tau^2 \mathbf{I}_n) \tag{5}$$

where $\mathbf{I}_n$ is the identity matrix of size n, and the variance–covariance matrix $\boldsymbol{\Sigma}(\boldsymbol{\theta})$ can be computed by evaluating $C(\mathbf{z}; \boldsymbol{\theta})$ for each pair of locations in $\mathcal{S}$, that is,

$$\boldsymbol{\Sigma}(\boldsymbol{\theta}) = \mathbf{C}_{n,n}(\boldsymbol{\theta}) = [C(\mathbf{s}_i, \mathbf{s}_j; \boldsymbol{\theta})]_{i,j=1:n}$$

We next specify prior distributions for the model parameters $\boldsymbol{\Omega}$, independently for $\{\boldsymbol{\beta}, \boldsymbol{\theta}, \tau^2\}$, as:

$$p(\boldsymbol{\Omega}) = p(\boldsymbol{\beta}) \times p(\sigma^2) \times p(\lambda_P) \times p(\lambda_v) \times p(\tau^2) \tag{6}$$

where $p(\cdot)$ denotes the marginal prior distribution of each parameter.

Careful selection of the marginal prior distributions $p(\cdot)$ for different model parameters is an important step in Bayesian estimation. More specifically, conjugate priors (distributions that belong to the same family of the posterior distribution) provide practical and computational advantages [74]. It is often recommended in Bayesian inference to assign Inverse-Gamma conjugate prior distributions for variance parameters (σ^2 and τ^2 in our model) and multivariate normal conjugate prior distributions for regression coefficients $\boldsymbol{\beta}$ [74,73]. With these choices, it can be shown

that the posterior conditional distribution of $\boldsymbol{\beta}$ is multivariate normal, $p(\boldsymbol{\beta}|\cdot) \sim MVN(\boldsymbol{\mu}_{\boldsymbol{\beta}|\cdot}, \boldsymbol{\Sigma}_{\boldsymbol{\beta}|\cdot})$, with its covariance matrix and mean vector given by Eqs. (7) and (8) [73],

$$\boldsymbol{\Sigma}_{\boldsymbol{\beta}|\cdot} = (\boldsymbol{\Sigma}_0^{-1} + \mathbb{X}^\top(\boldsymbol{\Sigma}(\boldsymbol{\theta}) + \tau^2\mathbf{I}_n)^{-1}\mathbb{X})^{-1} \tag{7}$$

$$\boldsymbol{\mu}_{\boldsymbol{\beta}|\cdot} = \boldsymbol{\Sigma}_{\boldsymbol{\beta}|\cdot}(\boldsymbol{\Sigma}_0^{-1}\boldsymbol{\mu}_0 + \mathbb{X}^\top(\boldsymbol{\Sigma}(\boldsymbol{\theta}) + \tau^2\mathbf{I}_n)^{-1}\mathbf{Y}) \tag{8}$$

where $\boldsymbol{\mu}_0$ and $\boldsymbol{\Sigma}_0$ are the mean vector and covariance matrix, respectively, of the prior distribution of $\boldsymbol{\beta}$. Since we do not have strong prior information regarding the remaining parameters λ_P and λ_ν, we select uniform prior distributions.

Finally, we use Markov Chain Monte Carlo simulation (MCMC) to updating posterior samples of model parameters. In particular, we use Gibbs sampler for parameters with a closed form conditional posterior distribution, and Metropolis–Hastings algorithm for the parameters whose posterior is not explicitly known [74]. Both point estimations and error estimations of model parameters are then conveniently obtained by summarizing key statistics such as posterior mean, posterior standard deviation and posterior credible intervals based on posterior samples.

5. Spatial prediction

The next step after estimating the model parameters is to use the estimates to make predictions of the porosity $Y(\mathbf{s})$ at any desired location $\mathbf{s}$.

More specifically, we seek to compute the posterior predictive distribution of $Y(\mathbf{s}_0)$ at an arbitrary location $\mathbf{s}_0$ given the observed data $\mathbf{Y}$ and the estimated model parameters $\boldsymbol{\Omega}$. It can be shown that this predictive distribution, $p(Y(\mathbf{s}_0)|\boldsymbol{\Omega}, \mathbf{Y})$, is normal with the following mean and variance [73]:

$$\mathrm{E}[Y(\mathbf{s}_0)|\boldsymbol{\Omega}, \mathbf{Y}] = \mathbf{X}(\mathbf{s}_0)\boldsymbol{\beta} + \mathbf{h}^\top(\mathbf{s}_0)(\boldsymbol{\Sigma}(\boldsymbol{\theta}) + \tau^2\mathbf{I}_n)^{-1}(\mathbf{Y} - \mathbb{X}\boldsymbol{\beta}) \tag{9}$$

where $\mathbf{X}(\mathbf{s}_0)$ are the spatially referenced predictors at $\mathbf{s}_0$, and $\mathbf{h}(\mathbf{s}_0) = (C(\mathbf{s}_0, \mathbf{s}_1; \boldsymbol{\theta}), \ldots, C(\mathbf{s}_0, \mathbf{s}_n; \boldsymbol{\theta}))^\top$ is the covariance vector between the new location $\mathbf{s}_0$ and each of the n observed locations. This posterior predictive mean is the same as the spatial best linear unbiased prediction (BLUP) estimator, commonly known as the Kriging mean.

The variance of the predictive distribution is defined as:

$$\mathrm{Var}[Y(\mathbf{s}_0)|\boldsymbol{\Omega}, \mathbf{Y}] = C(\mathbf{s}_0, \mathbf{s}_0; \boldsymbol{\theta}) + \tau^2 - \mathbf{h}^\top(\mathbf{s}_0)(\boldsymbol{\Sigma}(\boldsymbol{\theta}) + \tau^2\mathbf{I}_n)^{-1}\mathbf{h}(\mathbf{s}_0) \tag{10}$$

We remark that the results in Eqs. (9) and (10) not only provide a powerful tool for prediction but also can be used for model validation and model improvement via preferential sampling. Specifically, we can perform predictions at the observed locations and then compare the fitted values with actual observations to evaluate how well the model explains the physical experiment. In addition, we can improve prediction performance by sequentially selecting sampling points on the $P - \nu$ two-dimensional space. One effective strategy is to produce a predictive map of porosity based on the data collected from an initial experiment, and choose additional sampling points at those locations with high initial prediction errors to maximize information gain. Model fitting and preferential sampling based on prediction can be done in an interactive and sequential way to achieve optimal prediction performance.

The diagram in Fig. 1 visually summarizes our prediction methodology.

6. Case study

The predictive methodology outlined in Sections 3–5 is demonstrated using real-world data generated from the selective laser melting of 17-4 PH stainless steel. Test coupons of size 10 mm × 10 mm × 10 mm were produced on a ProX 100™ by 3D systems (Fig. 2). The system is equipped with a laser beam having a Gaussian profile and wavelength λ = 1070 nm, beam spot size of approximately 70 μm-diameter, and a maximum power of 50 W. Argon was used as inert protective atmosphere during fabrication.

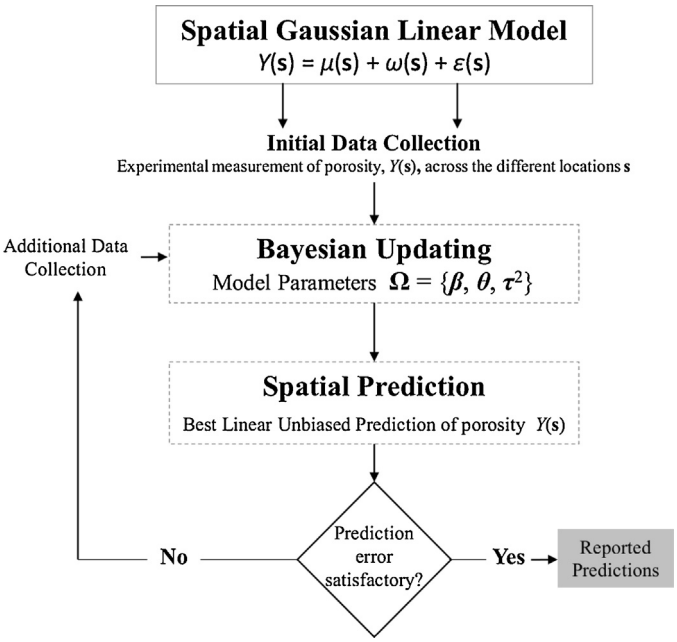

Fig. 1. Summary of the predictive methodology.

6.1. Production and measurement of test parts

As explained in Section 3, we focus on the effect of laser power and scanning speed on the porosity of the test coupons while maintaining the hatch distance and layer thickness constant at 50 μm and 30 μm, respectively. These values are the manufacturer recommended settings when processing 17-4 PH stainless steel. We do not have control on the beam size for our machine, so that is a fixed property as well. A 10-by-10 grid on the considered $P - \nu$ space was devised with the following configuration:

- Laser power: from $P = 40$ to 50 W, in 1 W steps.
- Laser scanning speed: from $\nu = 275$ to 400 mm/s, in 12.5 mm/s steps.

These ranges where selected based on several points: the limitations of our system to a maximum power of 50 W, inclusion of manufacturers default values into the study region, and to ensure bonding between layers of samples by avoiding extremely low powers or very fast speeds. The power and speed values described in this study are set on the manufacturing software of the commercial SLM system used.

The raw powder is 17-4 PH stainless steel by 3D systems. The powder was produced using gas atomization, and Table 1 shows its chemical composition. The particle size distribution is 10 μm < D50 < 13.5 μm and D80 < 22 μm, where D*xx* means *xx*% of the particles in a batch of powder. The coupons were built on a

Table 1
Chemical composition of the 17-4 PH stainless steel powder.

Element	Fe	Cr	Ni	HC Cu
Concentration (%)	70–80	10–25	1.0–10	1.0–10

(a)

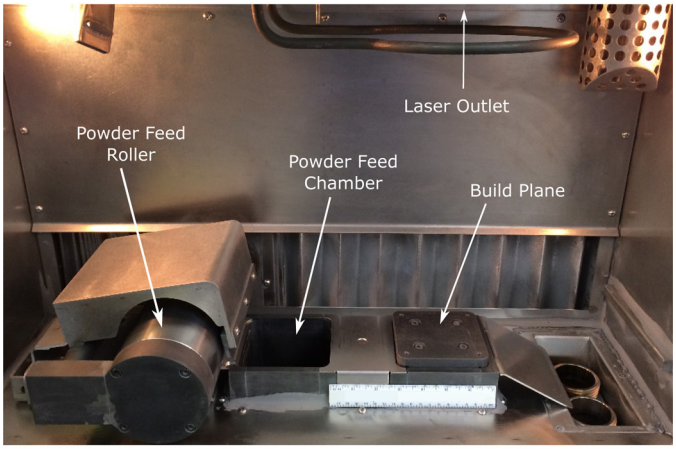

(b)

Fig. 2. (a) ProX 100^{TM} SLM system. (b) Inside view of the machine build chamber.

substrate made of 430F Stainless Steel. Fig. 3 shows 8 as-built test coupons prior to using electrical discharge machining (EDM) to cut them from the substrate.

The porosity (or density) of the test parts were then measured using the Archimedes' principle according to the standard ASTM B962-14 [75]. This is a classical method that has been previously used to determine the density of additively manufactured parts [76]. It is important to note that the method is sensitive to some factors such as precision of the balance, buoyancy of air, the relation between density and temperature of the liquid, surface tension of the liquid and presence of bubbles. To account for these factors in the current study, we used a balance with ±0.0001 g tolerance was used. Samples were put under vacuum to ensure no air bubbles are present when taking measurements and a correction factor was used for the volume of the float. In [77], it is reported that

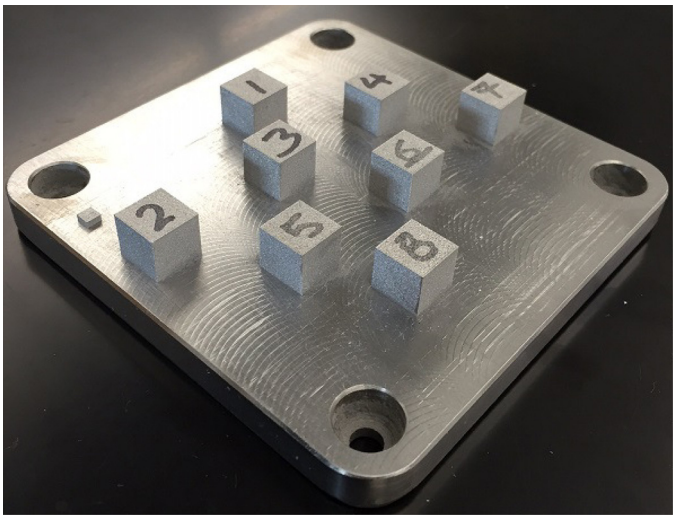

Fig. 3. As-built test coupons.

accounting for these factors resulted in ±0.08% accuracy in density measurements.

6.2. Preliminary data analysis

Forty-two coupons were initially built, each with a different power–speed combination, representing one data point on the defined grid. The first 30 points where chosen following a Latin hypercube design sampling, while the last 12 where chosen manually to fill in blank spaces in the study domain in order to reduce inter and extrapolation error in some areas. The observed porosities for these 42 coupons is displayed in Fig. 4(a). Evidence of spatial behavior can be observed in this plot, where higher values of porosity are in the top left quarter and lower values in the opposite quarter. Furthermore, to validate the assumption that the response follows a normal distribution (see Eq. (5)), we use a normal Q–Q plot, presented in Fig. 4(b), demonstrating that the data closely falls on the normality line.

6.3. Estimation of model parameters

Based on the discussion regarding the selection of prior distributions for the model parameters in Section 4, the following distributions were selected:

$p(\sigma^2)\sim$inv. gamma$(2, 1)$

$p(\tau^2)\sim$inv. gamma$(2, 0.2)$

$p(\boldsymbol{\beta})\sim$MVN$(0, 10^4\mathbf{I})$

$p(\lambda_P)\sim$uniform$(0, 10)$

$p(\lambda_v)\sim$uniform$(0, 125)$

Here, we assign vague (non-informative) inverse gamma prior distributions with shape parameter set equal to 2 for both σ^2 and τ^2. This conjugate prior specification has infinite variance and is hence a popular prior choice to let the data speak for itself. We also assign a vague multivariate normal distribution for $\boldsymbol{\beta}$: its zero mean gives no evidence whether the explanatory variables corresponding to the coefficients are strong enough to be considered in the model, and the diagonal covariance matrix with large diagonal entries gives no correlation among them and a very large variance for each covariate coefficient. Finally, the uniform priors are just non-informative flat distributions between values based on the selected range for each process parameter (power and scan speed).

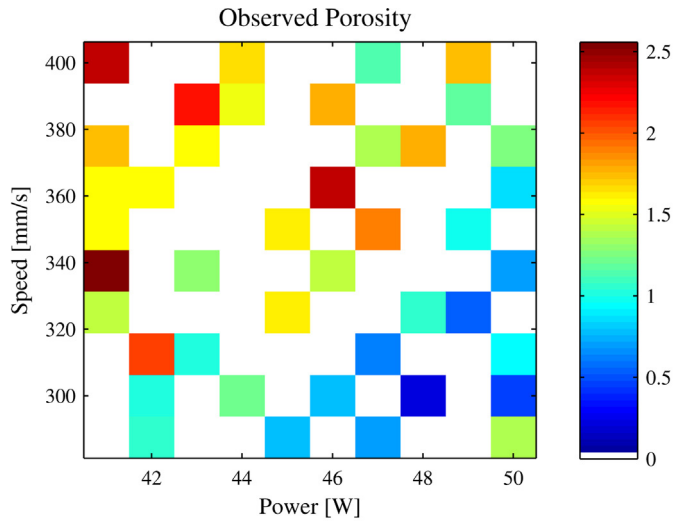

(a)

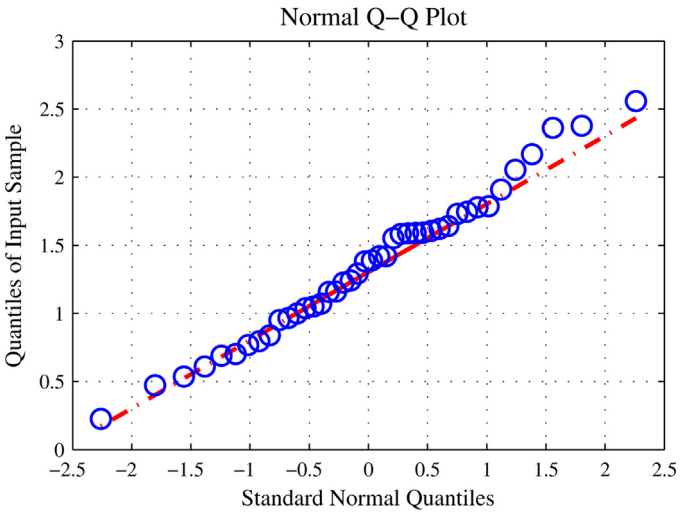

(b)

Fig. 4. Initial analysis of the data. (a) Spatial behavior of the observations across the grid. A white value means no observation in that location. (b) normal Q–Q plot for the initial data.

To start the estimation process, the value of the smoothness parameter of the Matérn covariance function was set to $\kappa = 1/2$. We continue by estimating the parameters $\boldsymbol{\beta} = (\beta_0, \beta_1, \beta_2, \beta_3, \beta_4, \beta_5)^\top$ using a Gibbs sampler. For estimation of the other model parameters, we employed the Metropolis–Hastings algorithm, with a truncated normal density as proposal distribution. The simulation was executed for 50,000 iterations with a burn-in period equal to 25% of the iterations. After initial runs, the parameters β_3, β_4, β_5 returned values almost equal to zero, and were thus omitted and the mean function was modeled as:

$$\mu(\mathbf{s}) = \beta_0 + \beta_1 x_P + \beta_2 x_v$$

With this modification, the simulation procedure was repeated, resulting in the posterior quantiles shown in Table 2.

Some intuitive observations are evident on inspecting the results in Table 2. First, β_1, the regression coefficient for the laser power coordinate, tends to have a negative value with a high probability, while β_2, the regression coefficient of the scanning speed coordinate, tends to have positive values. In other words, porosity decreases with higher laser power and increases with higher scanning speed. This is consistent with the well known expression for the energy density in SLM given by $E = P/v \cdot h_s \cdot t$ [78,79,54,23], where h_s is the hatch distance and t is the layer thickness. More specifically, the amount of energy deposited into the powder bed increases with higher laser power resulting in better powder melting and subsequent densification, and vice versa with higher scanning speed.

Table 2
Quantiles of the model parameters posterior distributions. Data was normalized prior simulations.

Parameter	Quantiles		
	2.5%	50%	97.5%
β_0	0.698	1.372	2.047
β_1	−0.601	−0.232	0.142
β_2	−0.123	0.238	0.577
σ^2	0.127	0.274	0.640
τ^2	0.043	0.090	0.169
λ_P	0.578	2.093	2.818
λ_v	0.576	2.093	3.029

The simulations for $\boldsymbol{\beta}$ and variance parameters seem to have converged, however, λ_P does not have a good convergence and varies around the whole domain for almost the whole run. This problem can have its reasons back to the original data set, as the number of observations ($n = 42$) might be relatively small in order to have good enough estimations.

6.4. Spatial prediction

In this step, we predict porosity over the considered $P - v$ space using Eqs. (9) and (10). Fig. 5(a) and (b) shows the predicted porosity and the associated standard error (SE), respectively. SE is computed by taking the square root of the MSE calculated by Eq. (10). The white dots in Fig. 5(b) represent the original observed data points. This plot demonstrates consistency of the predictive methodology since the error is expected to be small in locations that are closer to the observed data and larger at unobserved locations.

6.5. Model improvement

It can be seen in Fig. 5(b) that some locations have relatively high standard errors. To improve predictions, new observations were produced at several locations selected from both highest SE location and to fill in some regions in the space. These new observations were appended to the original data set, therefore the new dataset size was increased to 82 data points. The final number of observations was based on the number of regions with high error, empty regions with almost no observations, the range of the experiment space and the capabilities of the machine (since parameters can only take integer or half values).

Subsequently, procedure in Sections 4 and 5 was repeated with results shown in Fig. 6. The plot demonstrates that the new observations significantly reduced the SE. Both Figs. 5b and 6c are plotted under the same color scale, such that comparisons are easier to make. Although high SE areas can still be observed, they are mostly located on the boundaries of the study space where extrapolation is likely to happen. Gaussian processes are characterized by wider error bands in regions with fewer nearby points, such as boundaries, due to the intrinsic fact of having less neighborhood information to do inference and prediction [31,26].

This approach can be seen as an adaptive sampling method where we choose to observe new samples based on a condition that will improve the model. In this case, we choose locations that showed high SE such that uncertainty in predictions would be reduced after observing them.

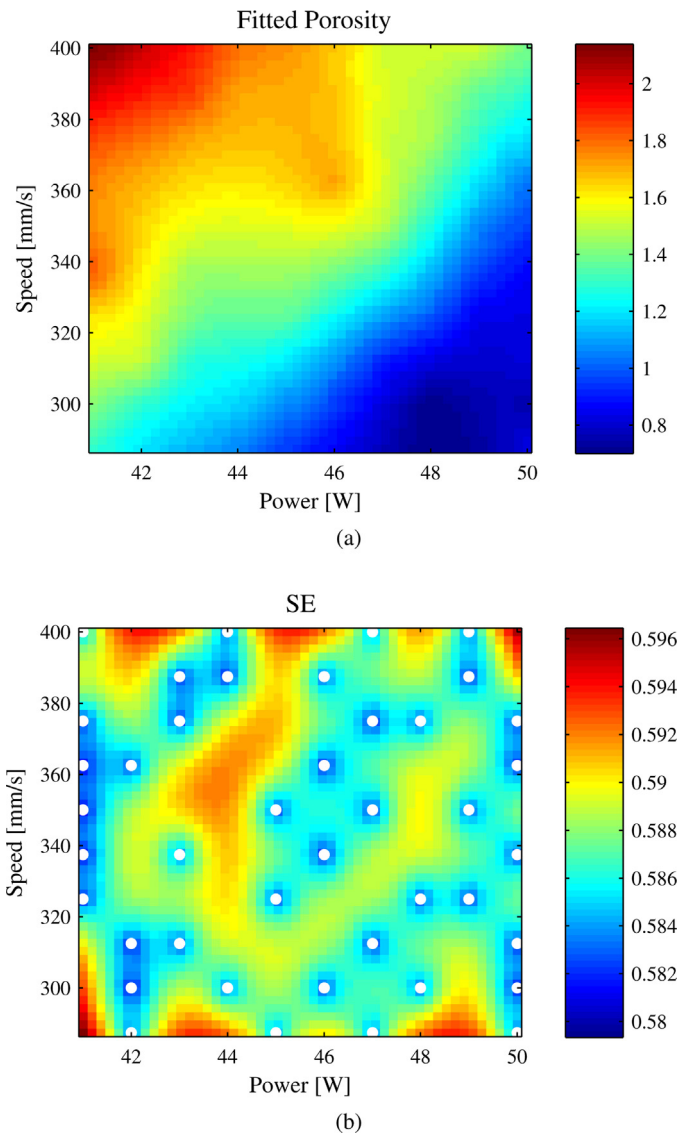

Fig. 5. Prediction results in the defined spatial range. (a) Fitted (predicted) porosity calculated by BLUP. (b) Prediction standard error for the predicted values. The white dots represent the locations of the initially observed data points.

6.6. *Cross validation*

To finalize the case study, we do a formal cross validation of the model as a measure of its predictive power outside the training set. Specifically we use a leave-one-out cross validation method using the whole dataset.

In cross validation, we define the generalizing error on model f, or mean-squared prediction error (MSPE), following equation (11).

$$\begin{aligned} \text{MSPE}_{\text{test}} &= \frac{1}{n}\sum_{i=1}^{n}(y_i - f_{(-i)}(\mathbf{s}_i))^2 \\ &= 0.2593 \end{aligned} \tag{11}$$

where $f_{(-i)}(\mathbf{s}_i)$ is the predicted value at location $\mathbf{s}_i$ of the model fitted by the whole dataset except for the ith location.

The calculated MSPE is a relatively low value for the generalizing error in the model, being about 20% of the range of the original observations. This means that the model does capture the process from the dataset and is able to explain and generalize it to unseen locations.

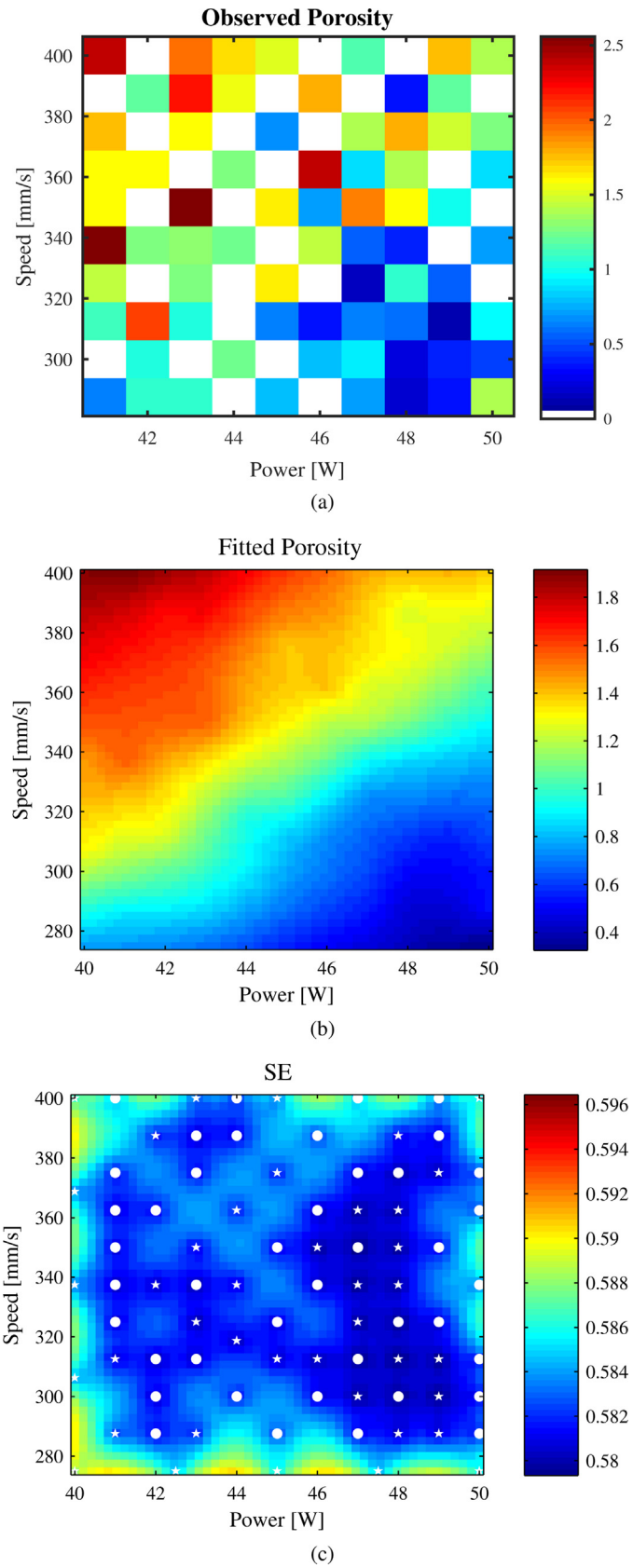

Fig. 6. Results after the addition of new data points. (a) New experimental observations added to the original dataset. (b) Predicted porosity. (c) Predicted SE. White stars show the location of the new additional observations.

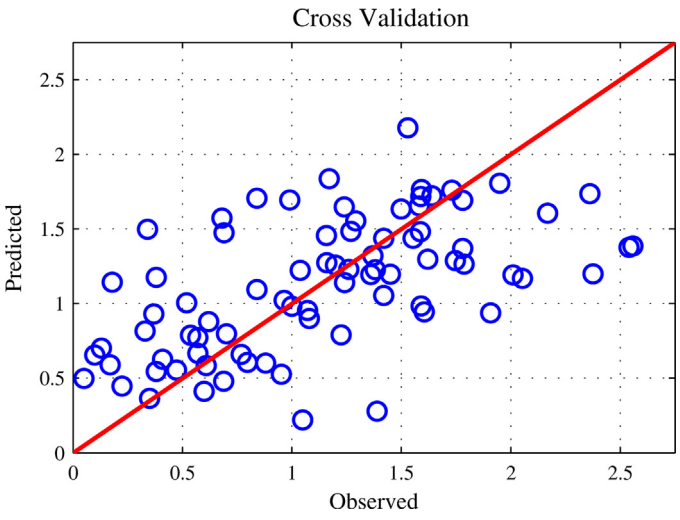

Fig. 7. Predictions for the cross-validated model.

Fig. 7 presents a plot comparing predicted and observed values for the cross-validated model. An ideal model would place all predictions over the red diagonal line, however we can see points from our model following the line closely.

7. Conclusions

Although AM has arguably existed since the early 1980s, its recent transformation from producing visualization or functional prototypes to manufacturing parts for end-use has contributed to the increased attention it recently received both among researchers and practitioners. This has resulted in more research needs in order to increase the manufacturing readiness level (MRL) of metal-based AM. There is a strong need for developing tools that provide predictive capabilities correlating manufacturing processing parameters with final part properties. In this paper, we developed a spatial statistics-based predictive framework to predict the porosity of metallic parts produced using SLM, a laser-based AM process. More specifically, we formulated a Gaussian process-based predictive model that expresses the porosity of the fabricated part as a function of laser power and scanning speed, which have been identified in the literature as two of the most influential processing parameters on part porosity. In our model, we use re-parameterization to extend the use of spatial covariance functions from their somewhat limited application in geographical spaces to generalized 2-dimensional spaces with different physical units (power and speed, in our study). A Bayesian updating methodology was used to estimate the parameters of the statistical model, and then best linear unbiased prediction (BLUP), commonly known as Kriging, was employed to predict the resulting porosity at any desired power-speed combination.

The majority of the works in the literature attempt to determine optimal processing parameter settings for achieving full density in the manufactured parts using intensive experimentation. In contrast to these works, we offer a systematic approach that enhances the determination of these parameter settings while keeping the number of experiments to a minimum, and thus saving time and cost. Our proposed methodology was validated using a real-world case study of predicting the porosity of 17-4 PH stainless steel specimens manufactured on a ProX 100^{TM} SLM system. The case study demonstrated that the methodology provides accurate predictions of part porosity under any parameter setting of interest. Furthermore, results from the case study accomplished the objective of finding parameter combinations that result in low porosity of 0.325% at $P = 50$ W and $v = 275$ mm/s.

The current work represents a study on data-driven prediction in metal-based AM. One important aspect to mention is the fact that metal-based AM is characterized by low repeatability due to the complexity of the underlying physical transformations that take place during fabrication. We attempt to capture this through evaluating the mean square error in predictions, however improving the repeatability of additively manufactured parts remains to be an important research direction. Other directions for future research include generalizing the model to a higher dimensional space accounting for additional SLM processing parameters (e.g. hatch distance, layer thickness, among others) and considering the effect of the characteristics of the raw powder (e.g. powder morphology, particle size distribution, fabrication procedure) on the part porosity.

Acknowledgements

The research of H. Sang is partially supported by NSF Grant CNS-1343155.

References

[1] I.J. Petrick, T.W. Simpson, 3D printing disrupts manufacturing, Res. Technol. Manag. 56 (6) (2013) 12–16.
[2] T. Campbell, C. Williams, O. Ivanova, B. Garrett, Could 3D Printing Change the World? Technologies, Potential, and Implications of Additive Manufacturing. Strategic Foresight Report, Atlantic Council, Washington, DC, 2011, Available from http://www.atlanticcouncil.org/images/files/publication_pdfs/403/101711_ACUS_3DPrinting.PDF.
[3] B. Berman, 3-D printing: the new industrial revolution, Bus. Horiz. 55 (2) (2012) 155–162.
[4] M. Averyanova, E. Cicala, P. Bertrand, D. Grevey, Experimental design approach to optimize selective laser melting of martensitic 17-4 PH powder. Part I: Single laser tracks and first layer, Rapid Prototyp. J. 18 (1) (2012) 28–37.
[5] A. Spierings, G. Levy, Comparison of density of stainless steel 316L parts produced with selective laser melting using different powder grades, in: Proceedings of the Solid Freeform Fabrication Symposium, Austin, TX, 2009, pp. 342–353.
[6] E. Yasa, J.-P. Kruth, Microstructural investigation of selective laser melting 316L stainless steel parts exposed to laser re-melting, Proc. Eng. 19 (2011) 389–395.
[7] S. Leuders, M. Thöne, A. Riemer, T. Niendorf, T. Tröster, H. Richard, H. Maier, On the mechanical behaviour of titanium alloy TiAl6V4 manufactured by selective laser melting: fatigue resistance and crack growth performance, Int. J. Fatigue 48 (2013) 300–307.
[8] B. Van Hooreweder, D. Moens, R. Boonen, J.-P. Kruth, P. Sas, Analysis of fracture toughness and crack propagation of Ti6Al4V produced by selective laser melting, Adv. Eng. Mater. 14 (1–2) (2012) 92–97.
[9] W.E. Frazier, Metal additive manufacturing: a review, J. Mater. Eng. Perform. 23 (6) (2014) 1917–1928.
[10] T. Wohlers, Wohlers Report 2013: Additive Manufacturing and 3D Printing State of the Industry-Annual Worldwide Progress Report, Wohlers Associates. Fort Collins Inc., 2013.
[11] M.J. Foust, D. Thomsen, R. Stickles, C. Cooper, W. Dodds, Development of the GE aviation low emissions TAPS combustor for next generation aircraft engines, in: 50th AIAA Aerospace Sciences Meeting Including the New Horizons Forum and Aerospace Exposition 936, 2012.
[12] C. Holshouser, C. Newell, S. Palas, C. Duty, L. Love, V. Kunc, R. Lind, P. Lloyd, J. Rowe, R. Dehoff, W. Peter, et al., Out of bounds additive manufacturing, Adv. Mater. Process. 171 (2) (2013 Mar) 15–17.
[13] J. Sundseth, J. Berg-Johnsen, Prefabricated patient-matched cranial implants for reconstruction of large skull defects, J. Cent. Nerv. Syst. Dis. 5 (2013) 19.
[14] L. Mullen, R.C. Stamp, W.K. Brooks, E. Jones, C.J. Sutcliffe, Selective laser melting: a regular unit cell approach for the manufacture of porous, titanium, bone in-growth constructs, suitable for orthopedic applications, J. Biomed. Mater. Res. B: Appl. Biomater. 89 (2) (2009) 325–334.
[15] D. Leordean, C. Dudescu, T. Marcu, P. Berce, N. Balc, Customized implants with specific properties, made by selective laser melting, Rapid Prototyp. J. 21 (1) (2015) 98–104.
[16] D.L. Bourell, M.C. Leu, D.W. Rosen, Roadmap for Additive Manufacturing: Identifying the Future of Freeform Processing. Progress Report, Laboratory of Freeform Fabrication, The University of Texas at Austin, 2009, Available from http://wohlersassociates.com/roadmap2009.pdf.
[17] National Institute of Standards and Technology (NIST), Measurement Science Roadmap for Metal-Based Additive Manufacturing, NIST, Workshop Summary Report, 2013, Available from http://www.nist.gov/el/isd/upload/NISTAdd_Mfg_Report_FINAL-2.pdf.
[18] D.L. Bourell, D.W. Rosen, M.C. Leu, The roadmap for additive manufacturing and its impact, 3D Print. Addit. Manuf. 1 (1) (2014) 6–9.

[19] G. Tapia, A. Elwany, A review on process monitoring and control in metal-based additive manufacturing, J. Manuf. Sci. Eng. 136 (6) (2014) 060801.
[20] J. Rudy, E. Rupert, Effects of porosity on mechanical properties of aluminum welds, Weld. J. 49 (7) (1970) 322.
[21] A. Bauereiß, T. Scharowsky, C. Körner, Defect generation and propagation mechanism during additive manufacturing by selective beam melting, J. Mater. Process. Technol. 214 (11) (2014) 2522–2528.
[22] S. Aqida, M. Ghazali, J. Hashim, Effect of porosity on mechanical properties of metal matrix composite: an overview, J. Teknol. 40 (1) (2012) 17–32.
[23] I. Gibson, D.W. Rosen, B. Stucker, et al., Additive Manufacturing Technologies, Springer, 2010.
[24] J.-P. Kruth, L. Froyen, J. Van Vaerenbergh, P. Mercelis, M. Rombouts, B. Lauwers, Selective laser melting of iron-based powder, J. Mater. Process. Technol. 149 (1) (2004) 616–622.
[25] M. Van Elsen, Complexity of Selective Laser Melting: A New Optimisation Approach, Ph.D. Dissertation, Katholieke Universiteit Leuven, 2007.
[26] R.A. Davis, Stochastic Modeling and Environmental Change, on Encyclopedia of Environmetrics, in: Gaussian Processes, Wiley, New York, 2001.
[27] S. Banerjee, B.P. Carlin, A.E. Gelfand, Hierarchical Modeling and Analysis for Spatial Data, CRC Press, 2014.
[28] M.C. Kennedy, A. O'Hagan, Bayesian calibration of computer models, J. R. Stat. Soc. Ser. B: Stat. Methodol. (2001) 425–464.
[29] J. Oakley, A. O'Hagan, Bayesian inference for the uncertainty distribution of computer model outputs, Biometrika 89 (4) (2002) 769–784.
[30] E.B. Sudderth, M.I. Jordan, Shared segmentation of natural scenes using dependent Pitman-Yor processes, in: Advances in Neural Information Processing Systems, 2009, pp. 1585–1592.
[31] C.E. Rasmussen, C.K.I. Williams, Gaussian Processes for Machine Learning, The MIT Press, 2006.
[32] American Society of Testing Materials, ASTM F2792 – 12a: Standard Terminology for Additive Manufacturing Technologies, ASTM, Standard, 2012, Available from http://www.astm.org/Standards/F2792.htm.
[33] D. Gu, Y.-C. Hagedorn, W. Meiners, G. Meng, R.J.S. Batista, K. Wissenbach, R. Poprawe, Densification behavior, microstructure evolution, and wear performance of selective laser melting processed commercially pure titanium, Acta Mater. 60 (9) (2012) 3849–3860.
[34] C. Fu, Y. Guo, Three-dimensional temperature gradient mechanism in selective laser melting of Ti-6Al-4V, J. Manuf. Sci. Eng. 136 (6) (2014) 061004.
[35] D. Gu, F. Chang, D. Dai, Selective laser melting additive manufacturing of novel aluminum based composites with multiple reinforcing phases, J. Manuf. Sci. Eng. 137 (2) (2015) 021010.
[36] L. Thijs, K. Kempen, J.-P. Kruth, J. Van Humbeeck, Fine-structured aluminium products with controllable texture by selective laser melting of pre-alloyed AlSi10Mg powder, Acta Mater. 61 (5) (2013) 1809–1819.
[37] R. Mertens, S. Clijsters, K. Kempen, J.-P. Kruth, Optimization of scan strategies in selective laser melting of aluminum parts with downfacing areas, J. Manuf. Sci. Eng. 136 (6) (2014) 061012.
[38] C. Haberland, H. Meier, J. Frenzel, On the properties of Ni-rich NiTi shape memory parts produced by selective laser melting, in: ASME Conference on Smart Materials, Adaptive Structures and Intelligent Systems, American Society of Mechanical Engineers, 2012, pp. 97–104.
[39] K. Amato, S. Gaytan, L. Murr, E. Martinez, P. Shindo, J. Hernandez, S. Collins, F. Medina, Microstructures and mechanical behavior of Inconel 718 fabricated by selective laser melting, Acta Mater. 60 (5) (2012) 2229–2239.
[40] J. Cherry, H. Davies, S. Mehmood, N. Lavery, S. Brown, J. Sienz, Investigation into the effect of process parameters on microstructural and physical properties of 316L stainless steel parts by selective laser melting, Int. J. Adv. Manuf. Technol. 76 (5–8) (2014) 869–879.
[41] I. Tolosa, F. Garciandí a, F. Zubiri, F. Zapirain, A. Esnaola, Study of mechanical properties of AISI 316 stainless steel processed by selective laser melting, following different manufacturing strategies, Int. J. Adv. Manuf. Technol. 51 (5–8) (2010) 639–647.
[42] W.E. King, H.D. Barth, V.M. Castillo, G.F. Gallegos, J.W. Gibbs, D.E. Hahn, C. Kamath, A.M. Rubenchik, Observation of keyhole-mode laser melting in laser powder-bed fusion additive manufacturing, J. Mater. Process. Technol. 214 (12) (2014) 2915–2925.
[43] A.J. Pinkerton, L. Li, Direct additive laser manufacturing using gas-and water-atomised H13 tool steel powders, Int. J. Adv. Manuf. Technol. 25 (5) (2005) 471–479.
[44] R. Cottam, J. Wang, V. Luzin, Characterization of microstructure and residual stress in a 3D H13 tool steel component produced by additive manufacturing, J. Mater. Res. 29 (17) (2014) 1978–1986.
[45] C. Casavola, S. Campanelli, C. Pappalettere, Experimental analysis of residual stresses in the selective laser melting process, in: Proceedings of the XIth International Congress and Exposition, Society for Experimental Mechanics Inc, Orlando, FL, 2008.
[46] K. Kempen, E. Yasa, L. Thijs, J.-P. Kruth, J. Van Humbeeck, Microstructure and mechanical properties of selective laser melted 18Ni-300 steel, Phys. Proc. 12 (2011) 255–263.
[47] K. Antony, Aging reactions in precipitation hardenable stainless steel, J. Metals 15 (1963) 922–927.
[48] C. Hsiao, C. Chiou, J. Yang, Aging reactions in a 17-4 PH stainless steel, Mater. Chem. Phys. 74 (2) (2002) 134–142.
[49] L. Facchini, N. Vicente, I. Lonardelli, E. Magalini, P. Robotti, A. Molinari, Metastable austenite in 17-4 precipitation-hardening stainless steel produced by selective laser melting, Adv. Eng. Mater. 12 (3) (2010) 184–188.
[50] S. Kumar, J.-P. Kruth, Wear performance of SLS/SLM materials, Adv. Eng. Mater. 10 (8) (2008) 750–753.
[51] L.E. Murr, S.M. Gaytan, D.A. Ramirez, E. Martinez, J. Hernandez, K.N. Amato, P.W. Shindo, F.R. Medina, R.B. Wicker, Metal fabrication by additive manufacturing using laser and electron beam melting technologies, J. Mater. Sci. Technol. 28 (1) (2012) 1–14.
[52] M. Averyanova, P. Bertrand, B. Verquin, Studying the influence of initial powder characteristics on the properties of final parts manufactured by the selective laser melting technology, Virtual Phys. Prototyp. 6 (December (4)) (2011) 215–223.
[53] A. Spierings, G. Levy, K. Wegener, Designing Material Properties Locally with Additive Manufacturing Technology SLM, ETH-Zürich, 2014.
[54] H. Gu, H. Gong, D. Pal, K. Rafi, T. Starr, B. Stucker, Influences of energy density on porosity and microstructure of selective laser melted 17-4PH stainless steel, in: Proceedings of Solid Freeform Fabrication Symposium, 2013, pp. 474–479.
[55] M. Averyanova, P. Bertrand, Direct manufacturing of dense parts from martensitic precipitation hardening steel gas atomized powder by selective laser melting (SLM) technology, in: 4th International Conference on Advanced Research in Virtual and Rapid Prototyping, Leiria, Portugal, 2009, pp. 343–348.
[56] A.E. Gelfand, P. Diggle, P. Guttorp, M. Fuentes, Handbook of Spatial Statistics, CRC Press, 2010.
[57] V. Nair, M. Hansen, J. Shi, Statistics in advanced manufacturing, J. Am. Stat. Assoc. 95 (451) (2000) 1002–1005.
[58] M.M. Fischer, A. Getis, Handbook of Applied Spatial Analysis: Software Tools, Methods and Applications, Springer Science & Business Media, 2009.
[59] T.-H. Yang, J. Jackman, Form error estimation using spatial statistics, J. Manuf. Sci. Eng. 122 (1) (2000) 262–272.
[60] B.M. Colosimo, Q. Semeraro, M. Pacella, Statistical process control for geometric specifications: on the monitoring of roundness profiles, J. Qual. Technol. 40 (1) (2008) 1–18.
[61] R.S. Collica, J.G. Ramirez, W. Taam, Process monitoring in integrated circuit fabrication using both yield and spatial statistics, Qual. Reliab. Eng. Int. 12 (3) (1996) 195–202.
[62] S.-C. Hsu, C.-F. Chien, Hybrid data mining approach for pattern extraction from wafer bin map to improve yield in semiconductor manufacturing, Int. J. Prod. Econ. 107 (1) (2007) 88–103.
[63] S. Pegel, P. Pötschke, T. Villmow, D. Stoyan, G. Heinrich, Spatial statistics of carbon nanotube polymer composites, Polymer 50 (9) (2009) 2123–2132.
[64] C. Kamath, B. El-dasher, G.F. Gallegos, W.E. King, A. Sisto, Density of additively-manufactured, 316L SS parts using laser powder-bed fusion at powers up to 400 W, Int. J. Adv. Manuf. Technol. 74 (1–4) (2014) 65–78.
[65] J.-P. Kruth, S. Kumar, J. Van Vaerenbergh, Study of laser-sinterability of ferro-based powders, Rapid Prototyp. J. 11 (5) (2005) 287–292.
[66] J.-P. Kruth, S. Kumar, Statistical analysis of experimental parameters in selective laser sintering, Adv. Eng. Mater. 7 (8) (2005) 750–755.
[67] S. Dingal, T. Pradhan, J.S. Sundar, A.R. Choudhury, S. Roy, The application of Taguchi's method in the experimental investigation of the laser sintering process, Int. J. Adv. Manuf. Technol. 38 (9–10) (2008) 904–914.
[68] D. Miller, C. Deckard, J. Williams, Variable beam size SLS workstation and enhanced SLS model, Rapid Prototyp. J. 3 (1) (1997) 4–11.
[69] A. Chatterjee, S. Kumar, P. Saha, P. Mishra, A.R. Choudhury, An experimental design approach to selective laser sintering of low carbon steel, J. Mater. Process. Technol. 136 (1) (2003) 151–157.
[70] B. Caulfield, P. McHugh, S. Lohfeld, Dependence of mechanical properties of polyamide components on build parameters in the SLS process, J. Mater. Process. Technol. 182 (1) (2007) 477–488.
[71] P.K. Jain, P.M. Pandey, P. Rao, Experimental investigations for improving part strength in selective laser sintering, Virtual Phys. Prototyp. 3 (3) (2008) 177–188.
[72] A. Simchi, Direct laser sintering of metal powders: mechanism, kinetics and microstructural features, Mater. Sci. Eng. A 428 (1) (2006) 148–158.
[73] H. Sang, J.Z. Huang, A full scale approximation of covariance functions for large spatial data sets, J. R. Stat. Soc. Ser. B: Stat. Methodol. 74 (1) (2012) 111–132.
[74] A. Gelman, J.B. Carlin, H.S. Stern, D.B. Rubin, Bayesian Data Analysis, Chapman & Hall/CRC, 2003.
[75] American Society of Testing Materials, ASTM B962-14: Standard Test Methods for Density of Compacted or Sintered Powder Metallurgy (PM) Products Using Archimedes' Principle, ASTM Standard, 2012, Available from http://www.astm.org/Standards/B962.htm.
[76] J.A. Slotwinski, E.J. Garboczi, K.M. Hebenstreit, Porosity measurements and analysis for metal additive manufacturing process control, J. Res. Natl. Inst. Stand. Technol. 119 (2014) 494.
[77] A. Spierings, M. Schneider, R. Eggenberger, Comparison of density measurement techniques for additive manufactured metallic parts, Rapid Prototyp. J. 17 (5) (2011) 380–386.
[78] L. Thijs, F. Verhaeghe, T. Craeghs, J. Van Humbeeck, J.-P. Kruth, A study of the microstructural evolution during selective laser melting of TI-6AL-4V, Acta Mater. 58 (9) (2010) 3303–3312.
[79] J. Ciurana, L. Hernandez, J. Delgado, Energy density analysis on single tracks formed by selective laser melting with CoCrMo powder material, Int. J. Adv. Manuf. Technol. 68 (5–8) (2013) 1103–1110.